

A comparison of hydrodynamic and thermal properties of artificially generated against realistic rough surfaces

Jiasheng Yang ^a, Juan Velandia ^{b,c}, Stephan Bansmer ^{b,c}, Alexander Stroh ^a, Pourya Forooghi ^{d,*}

^a Institute of Fluid Mechanics, Karlsruhe Institute of Technology, Kaiserstr.10, Karlsruhe, 76131, Germany

^b Institut für Strömungsmechanik, Technische Universität Braunschweig, Hermann-Blenk-Str.37, Braunschweig, 38108, Germany

^c Coldsense Technologies, Hermann-Blenk-Str.37, Braunschweig, 38108, Germany

^d Department of Mechanical & Production Engineering, Aarhus University, Katrinebjergvej 89G-F, Aarhus, 8200, Denmark

ARTICLE INFO

Keywords:

Ice accretion

Roughness

Direct numerical simulation

ABSTRACT

The mathematical roughness generation approaches enjoy outstanding flexibility in delivering desired roughness geometries to perform systematic research. However, whether an mathematically (artificially) generated roughness can be considered an adequate surrogate of a realistic surface in terms of its influence on the flow remains nonetheless an open question. Motivated by this, the present study discusses the possibility of reproducing flow properties over realistic roughness with artificial roughness. To this end, six types of artificial rough surfaces are generated through imitation of the realistic height probability density function (PDF) and the roughness power spectrum (PS) preserving the stochastic nature of the roughness structure. The flow properties of the artificial surfaces are assessed using direct numerical simulations (DNS) in a fully-developed turbulent channel flow at $Re_\tau = 500-2000$. An excellent match in terms of global flow properties, mean velocity and temperature profiles, Reynolds stresses as well as equivalent sand grain sizes is found compared to their original counterpart with exception of a strongly anisotropic sample (surface anisotropy ratio $SAR \approx 1.7$). Additionally, some artificial surfaces are generated by matching only the PS, and it was shown that only at adequately low effective slopes this can lead to similar flow properties. Overall, the results suggest that artificial roughness generated using the employed method by mimicking realistic PDF and PS can be applied as a full-fledged surrogate for realistic roughness under the premise of surface isotropy.

1. Introduction

Examples of rough surfaces are abundant in flow-related engineering applications, e.g. on degraded turbine blades (Bons et al., 2001), biofouled ship hulls (Sarakinis and Busse, 2022), deposit in combustion engines (Forooghi et al., 2018b) or ice accretion on aircraft surfaces (Bansmer, 2020). It is widely reported that the presence of roughness can compromise the performance of the equipment to a significant extent as roughness affects momentum and heat transfer in the near wall region (Chung et al., 2021). According to the outer-layer similarity hypothesis, proposed by Townsend (1976), the outer-layer turbulence is unaffected by the roughness structure under the circumstance of a significant separation of scales, i.e. $k \ll \delta$, where k measures the height of roughness and δ denotes the boundary layer height. When outer-layer similarity holds, a roughness-induced increase in drag coefficient translates to an offset in inner-scaled mean velocity profile in the logarithmic layer comparing to the smooth case (Jiménez, 2004). The amount of such an offset is denoted as (Hama) roughness function ΔU^+ (Hama and Society of Naval Architects and Marine Engineers,

1954). Analogous to the momentum transfer, an increase in the heat transfer capability of a surface due to roughness can be manifested as a retardation of the logarithmic inner-scaled temperature profile $\Delta \theta^+$ (Kader, 1981; Kawamura et al., 1999; Yaglom, 1979).

In realistic applications, roughness can appear in a variety of shapes and distributions. As widely reported, the roughness impact on the skin friction and heat transfer depends strongly on roughness morphology (Chung et al., 2021). In the present work, special attention is paid to roughness due to ice accretion, as an example of realistic roughness in which the morphology can be very different from one case to the other. A brief overview of this type of roughness is, hence, presented in the following. Atmospheric ice accretion can be regarded as a type of surface degradation leading to serious deterioration of equipment performance. For instance, the accumulation of ice on wind turbines can lead to the reduction of their power production (Yirtici et al., 2019). The aerodynamic performance, and consequently the flight safety, of an aircraft can be lowered due to ice accretion, making

* Corresponding author.

E-mail address: forooghi@mpe.au.dk (P. Forooghi).

deep understanding of roughness effect imperative. In an aircraft, the intake lip of the engine is particularly exposed to icing events during take-off or climb (Velandia and Bansmer, 2019). On the engine nacelle, different sections of ice accretion can be identified based on the ice morphology. Notably, spiky ice – or ice feathers – can be usually found locating at a certain distance from the stagnation region due to the coalescence and freeze of water beads, while relatively less prominent roughness features locate commonly close to the stagnation region due to frozen water film. Due to such variations in the iced surface properties, zonal analysis is commonly recommended for study of ice accretion effects (Anderson et al., 1998).

In the industrial applications, the Moody diagram (Moody, 1944) is usually used to predict the skin friction of a roughness. To this end, equivalent sand grain height k_s should be calculated from the rough surface of interest. The value of k_s for an arbitrary irregular roughness is not known *a priori* but can only be calculated from either laboratory experiments or simulations at fully rough regime. The fully rough regime represents a certain threshold of Reynolds number beyond which the skin friction coefficient exerted by the roughness is no more a function of the Reynolds number. Therefore, the value of k_s for an arbitrary roughness is Reynolds number independent. To calculate the k_s value of a interested roughness, simulating the roughness flow properties with canonical flow condition in fully developed turbulent channel driven by constant pressure gradient (CPG) is the standard practice. study of roughness with more complex flow conditions while being a significant research question, is out of the scope of the present work. It has been long desired to predict the k_s value solely based on the geometrical properties of a roughness. To this end, multiple statistical measures of roughness topographical features have been suggested to characterize the roughness, e.g. the roughness root-mean-square height k_{rms} , the roughness peak-to-trough height k_t , skewness Sk and effective slope ES (Flack and Schultz, 2010; Forooghi et al., 2017; Napoli et al., 2008; Chan et al., 2015). Despite the wide variety of statistical measures used for roughness characterization, a scatter of predicted roughness effect still exist. In other words, different surfaces with identical aforementioned statistics values exhibit considerable scatter of its roughness effect. For example, 30% disagreement of the k_s value is reported between the roughness whose statistics are same but with aligned or staggered arrangement of roughness elements (Forooghi et al., 2017).

Artificially generated roughness has been studied since the time of pioneering experiments by Nikuradse (1933) and Schlichting (1936) as it facilitates systematic understanding of the effects of roughness geometry and relaxes the need for realistic surface measurements. Many later studies made use of identical geometric roughness elements – such as cubes, cones and spheres – to study flow over rough surfaces (see e.g. Orlandi and Leonardi (2006), Chan-Braun et al. (2011)). Other authors attempted to generate roughness more closely resembling irregular, naturally-formed roughness by random placement of roughness elements with different sizes (Scotti, 2006; Forooghi et al., 2018a; Kuwata and Kawaguchi, 2019). Anderson and Meneveau (2011) used random Fourier modes to generate roughness with power-law roughness power spectrum (PS). Artificial roughness can also be generated by combining random numbers in a linear manner, as some authors have done (Barros et al., 2018; Jelly and Busse, 2019). Despite the fact that these methods provide great flexibility in realizing the desired PS for the roughness, they can only generate a Gaussian roughness height probability density function (PDF). In a recent study, Flack et al. (2020) used a modified version of these methods to investigate non-Gaussian roughness. With the aim of conducting a comprehensive study of roughness, a source of artificial roughness is desired, whose roughness effect can be uniquely determined by the input of the generation algorithm while the highest possible flexibility of varying the roughness properties is preserved. In the present work, we adopt a roughness generation method lately proposed by (Pérez-Ràfols and Almqvist, 2019). The advantage of this method, which will be described

Table 1

Summary of surface geometrical statistics. Units: mm.

Surface	Configuration	k_{md}	k_{rms}	k_t	Sk	Ku	ES	L_x^{Corr}	L_z^{Corr}	SAR
ICE1-R	Realistic	0.19	0.07	0.63	0.76	4.72	0.16	0.60	0.68	0.88
ICE1-A	Realistic PDF+PS	0.19	0.07	0.63	0.76	4.75	0.17	0.54	0.54	1.00
ICE1-G	Gaussian PDF+PS	0.30	0.07	0.64	0.00	3.00	0.18	0.54	0.54	1.00
ICE2-R	Realistic	0.09	0.03	0.28	1.17	6.39	0.13	0.64	0.56	1.14
ICE2-A	Realistic PDF+PS	0.09	0.03	0.28	1.18	6.46	0.11	0.50	0.52	0.96
ICE2-G	Gaussian PDF+PS	0.13	0.03	0.27	0.00	2.98	0.12	0.50	0.52	0.96
ICE3-R	Realistic	0.20	0.05	0.47	0.49	4.42	0.10	0.74	0.92	0.80
ICE3-A	Realistic PDF+PS	0.20	0.05	0.47	0.50	4.46	0.12	0.58	0.58	1.00
ICE3-G	Gaussian PDF+PS	0.23	0.05	0.44	0.01	3.00	0.11	0.58	0.58	1.00
ICE4-R	Realistic	0.26	0.17	0.98	1.87	5.73	0.40	0.64	0.38	1.68
ICE4-A	Realistic PDF+PS	0.25	0.17	0.97	1.88	5.74	0.34	0.40	0.40	1.00
ICE4-G	Gaussian PDF+PS	0.61	0.17	1.18	0.00	2.88	0.42	0.50	0.52	0.96
Sand-R	Realistic	0.65	0.09	1.16	0.77	3.80	0.48	0.29	0.30	1.03
Sand-A	Realistic PDF+PS	0.65	0.09	1.16	0.74	3.74	0.47	0.31	0.31	1.00
Sand-G	Gaussian PDF+PS	0.84	0.09	1.29	0.00	3.00	0.45	0.28	0.28	1.01
CCD-R	Realistic	0.23	0.20	1.72	3.02	12.3	0.32	0.86	0.76	1.13
CCD-A	Realistic PDF+PS	0.24	0.20	1.71	3.02	12.3	0.31	0.78	0.78	1.00

in details later, can be attributed to the possibility to gain robust and precise results for a flexible combination of PDF and PS.

One should bear in mind that mathematical (artificial) roughness generation methods seek to reproduce realistic surfaces in a geometric sense. This is done through mimicking certain statistical measures of the target roughness geometry (ranging from simply the mean roughness height to the complete PDF and PS in the works cited above). Whether or not this can lead to a similar dynamic (and thermal) effect on the flow is an open question that the current research attempts to address. Note that such a dynamic similarity is necessary if artificial roughness is to be used as a surrogate of realistic roughness for flow related applications. Specifically, the objective of the present study is to examine if an artificial roughness, generated through the named method, can mimic a realistic roughness with matched PDF and PS in terms of its impact on mean velocity and temperature profiles. To this end, we attempt to reproduce four different ice accretion roughness samples with distinctively different roughness morphologies and compare the flow response to both actual and reproduced samples through DNS in turbulent channel flow at otherwise similar conditions. To add to the range of studied roughness parameters, a combustion chamber roughness sample – originally reported in Forooghi et al. (2018b) – and a sandpaper surface have been examined in the same manner.

The paper is organized as follows. In Section 2 we describe the methodology for acquirement of realistic roughness as well as the reproduction of their artificial surrogates. Section 3 summarizes the results of the DNS of turbulent flow on roughness. Finally, the summary and conclusions are presented in Section 4.

2. Methodology

2.1. Acquisition of realistic roughness

As a starting point, the sandpaper roughness of ISO Grit P60 is adopted as a generic representation of realistic ‘naturally-occurring’ roughness, the corresponding roughness statistical metrics are specified in the Table 1. In the following content, roughness associated with sandpaper is labeled with the keyword *Sand*. Ice accretion roughness on a simplified aero-engine nacelle were generated in the Braunschweig Icing Wind Tunnel (Bansmer et al., 2018). The condition details of the tests set-up can be found in Velandia and Bansmer (2020). Testing reproduces the ice accretion process on a complex geometry in take-off conditions during glaze ice formation, which implies that the physics of drawing away a water film influences ice formation. A sketch of the ice geometry is shown in Fig. 1. The geometry of the nacelle leads to different local boundary conditions for the accretion process (such as local pressure, local air velocity and water film thickness). Such

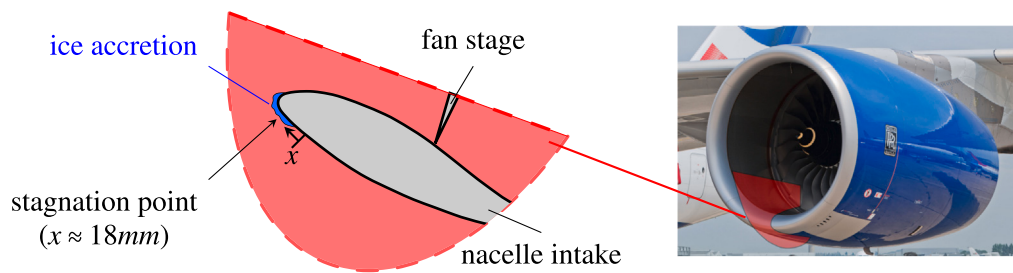


Fig. 1. Sketch of the ice accretion and location of the stagnation line ($x \approx 18 \text{ mm}$) on the aero-engine nacelle.

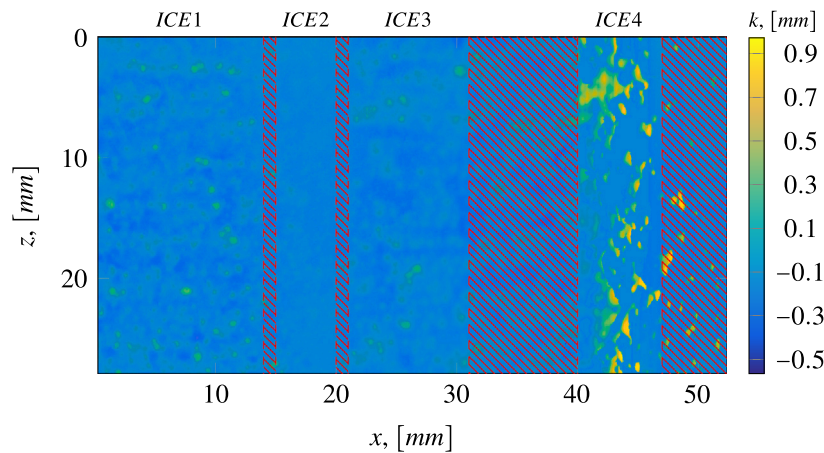


Fig. 2. Ice accretion roughness overview, the section *ICE2* corresponds to the stagnation region of the surface. Hatched patterns indicate transitional roughness structures.

differences produce an inhomogeneous surface with different roughness properties. The surface is unfolded considering the form of the nacelle model and the x -coordinate is used in the streamwise direction. Once unfolded, the surface can be divided into a relatively smooth region, on the stagnation line of the model and three different rough regions, away from the stagnation line as shown in Fig. 2. This is known as a roughness zonal model in the icing community (Anderson et al., 1998). Recalling the aim of the present work, the evaluation of roughness reproduction framework is carried out on the homogeneous roughness whose properties is invariant to the position. Therefore, homogeneous roughness patches are sought from the ice accretion roughness for the present study. The effective slope (ES) in the z -direction of Fig. 2 was used to differentiate these regions and produce different roughness patches with almost homogeneous characteristics. These surfaces are illustrated in Fig. 2. The differences in the surfaces characteristics respond to different in the physics of the ice accretion process. A relatively smooth section can be found at $x \approx 18 \text{ mm}$ located at the stagnation region. The growth of ice accretion is visible towards both suction side and pressure side. At the right end of the ice accretion surface spiky ice can be found. This zone is only reached by remaining of a water film or accumulates isolated water beads, which explains the formation of spiky structures. The homogeneous roughness section on the left end of the surface is named *ICE1* corresponding to the pressure side of the test model. *ICE2* corresponds to the stagnation area of the test model. *ICE3* and *ICE4* both lay on the suction side of the model but present different roughness characteristics. The last sample studied in this work is the *CCD* surface, which is extracted from the piston head of a single-cylinder research internal combustion engine under realistic operating condition. The roughness is adopted from the previous research by Forooghi et al. (2018b). More detailed description of these surfaces can be found in the original references. In the following parts of this paper, the four ice roughness sections as well as the *CCD* surface and the sandpaper surfaces will be characterized, artificially reproduced and their flow properties will be compared to the artificial counterparts (see Fig. 2).

2.2. Pseudo-random roughness generation

As is depicted in Fig. 5, the roughness in the simulation domain is represented by discrete wall elevation distribution on 2-D wall parallel coordinate, i.e. $k(x, z)$. Where x and z represents streamwise and spanwise coordinates, respectively. The roughness generation method proposed by Pérez-Ràfols and Almqvist (2019) is employed. An artificial surface is composed of multiple sinusoidal waves whose amplitudes and phases are iteratively adjusted to match the target PDF and PS. The transformation of roughness in frequency space is done by discrete fast Fourier transform (DFFT). For greater details on the generation algorithm, reader is referred to the original work (Pérez-Ràfols and Almqvist, 2019).

Artificial roughness is generated based on the PDF and PS associated with the realistic surfaces in the present study. As an example, the PDF and PS of the *Sand* surface scan are shown in Fig. 3 with gray marks while its artificial surrogate is represented by black marks. It is worth noting that, the PS of a 2-D signal is a surface in 2-D frequency space. The 1-D PS is obtained by radially accumulating the PS data points around its origin, i.e. around $(q_x, q_z) = (0, 0)$, as a function of wavelength $q = \sqrt{q_x^2 + q_z^2}$, where q_x and q_z represent the wavenumber in x and z direction, respectively. This 1-D PS is simply referred to as PS in the following text. The scatter of the PS in Fig. 3(b) is the evidence of the slight anisotropic nature of the realistic surface. In order to achieve isotropic roughness distribution, the PS is subjected to a radial averaging process around the origin (Jacobs et al., 2017). Subsequently, the moving average is applied along the PS in order to represent the realistic PS with a reduced level of complexity. Furthermore, low- and high-pass filters are applied to the surface PS to eliminate roughness structures with extremely large or small wavelengths. The selection of these values will be elaborated in the next section. The largest and the smallest roughness wavelength bounds are denoted as λ_0 and λ_1 in the following text, respectively. Eventually, the simplified PS of the artificial surface is shown with the black dots in Fig. 3(b).

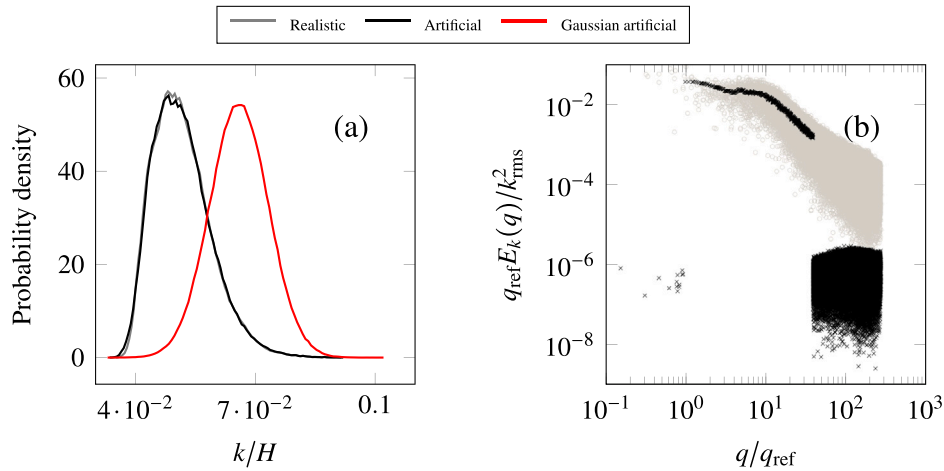


Fig. 3. Comparison of realistic and artificial sandpaper roughness PDF (a) and PS (b). Where $q_{ref} = 2\pi/\lambda_0$.

To understand the effect of PDF and PS in an isolated manner, in the present work, artificial surfaces with matched PS but not PDF are additionally produced and analyzed. For these artificial surfaces, a Gaussian PDF with identical standard deviation k_{rms} to the target surface is prescribed. Finally, the PDFs of realistic and artificial surfaces (including Gaussian PDF) are shown in Fig. 3(a). The artificial rough surfaces along with the original sandpaper scan are visualized in Fig. 4(a). In the following content, the realistic surfaces and the artificial surfaces utilizing realistic PDF are denoted by the abbreviations -R and -A, respectively. The Gaussian distributed artificial surfaces are labeled with -G.

Using the same procedure as above, the ICE1-4 and the CCD are reproduced. The substitution of Gaussian PDF is performed for ICE1-4 as well. These artificial surfaces are visualized in Fig. 4 (b–f) along with their original realistic surface scans. As is reflected in Fig. 4, characteristic roughness structures, such as the sediment-like roughness elements on the CCD-R, are successfully reproduced by the generation method. The statistical metrics for roughness are quantitatively compared in Table 1 and defined as

$$k_{md} = (1/S) \int_S k dS, \quad (1a)$$

$$k_{rms} = \sqrt{(1/S) \int_S (k - k_{md})^2 dS}, \quad (1b)$$

$$k_t = \max(k) - \min(k), \quad (1c)$$

$$ES = (1/S) \int_S |\partial k / \partial x| dS, \quad (1d)$$

$$Sk = \int_S (k - k_{md})^3 dS / k_{rms}^3, \quad (1e)$$

$$Ku = \int_S (k - k_{md})^4 dS / k_{rms}^4, \quad (1f)$$

$$SAR = L_x^{Corr} / L_z^{Corr}, \quad (1g)$$

where S is the wall-projected surface area. SAR represents surface anisotropy ratio (Busse and Jelly, 2020), L^{Corr} is the correlation length at which distance the auto-correlation function drops under 0.2. It is noticeable that there is a limited range of statistics values available in the current roughness data set. As discussed in the previous section, the roughness properties of a surface strongly depend on its background and forming mechanism. For this reason, no negatively skewed realistic roughness is currently available at our institute. In spite of this, the currently included surfaces already exhibit a considerable range of roughness properties in terms of Sk and ES that covers a considerable

parts of the previous studies (Napoli et al., 2008; Yuan and Piomelli, 2014; Kuwata and Kawaguchi, 2019; Chung et al., 2021). However, it must be stressed that over-generalization of the present results should be avoided. Among these statistics, it is clear that the values of k_{md} , k_{rms} , k_t as well as Sk and Ku are directly related to the configuration of PDF. The PS, however, is more complex since it accounts for the spatial distribution of roughness at various length scales. The value of ES is thus closely related to the PS. But it can be appreciated from the present data set and literature (Yang et al., 2022), that while the ES value is largely determined by PS, the impact of PDF cannot be ignored. The value of L^{Corr} , on the other hand, can be uniquely defined by PS because the auto-correlation function can be directly derived from PS through reverse Fourier transformation. However, as a matter of fact, the realistic roughness typically consists of a wide range of length scales which cannot be adequately described by a set of roughness statistics. The use of PS has advantage of reflecting the behavior of each roughness length scale. Therefore, PS is expected to provide a more comprehensive representation of roughness spatial distribution than the aforementioned roughness statistics. Based on this comparison, one can conclude that roughness topographical properties can be successfully reproduced by imitating the PS and PDF of the original surfaces. A slight deviation in the statistics can be observed, which might be attributed to the random nature of the generation process (Yang et al., 2022) as well as the averaging process of PS. In clear contrast to the different degrees of anisotropy exhibited by realistic surfaces – as is reflected by SAR (Busse and Jelly, 2020) – the artificial surfaces exhibit nearly perfect isotropic distribution with $SAR \approx 1$. Because of the strongly anisotropic roughness distribution of ICE4-R ($SAR \approx 1.7$), this results in the departure of the generated surface topography, for this surface. It can be seen from Fig. 4(e) that the anisotropic roughness elements of the surface ICE4-R are deformed into isotropic roughness elements through the roughness reproduction process. Likewise, the strip-like anisotropic valleys of CCD-R are transformed into isotropic pits in CCD-A.

Furthermore, the impact of the Gaussian PDF is evident if one compares the roughness statistics. In the present work, the PDFs of the considered roughness are all positively skewed, i.e. the majority of the roughness height is located below the roughness median height $k_t/2$. A symmetric height distribution around $k_t/2$ is obtained by substituting Gaussian PDF, which results in a lift of the roughness melt-down height k_{md} . Moreover, it is worth noting that while the other statistical measurements appears to be influenced by the variation in PDF configuration, ES is less susceptible to this variation (see Table 4).

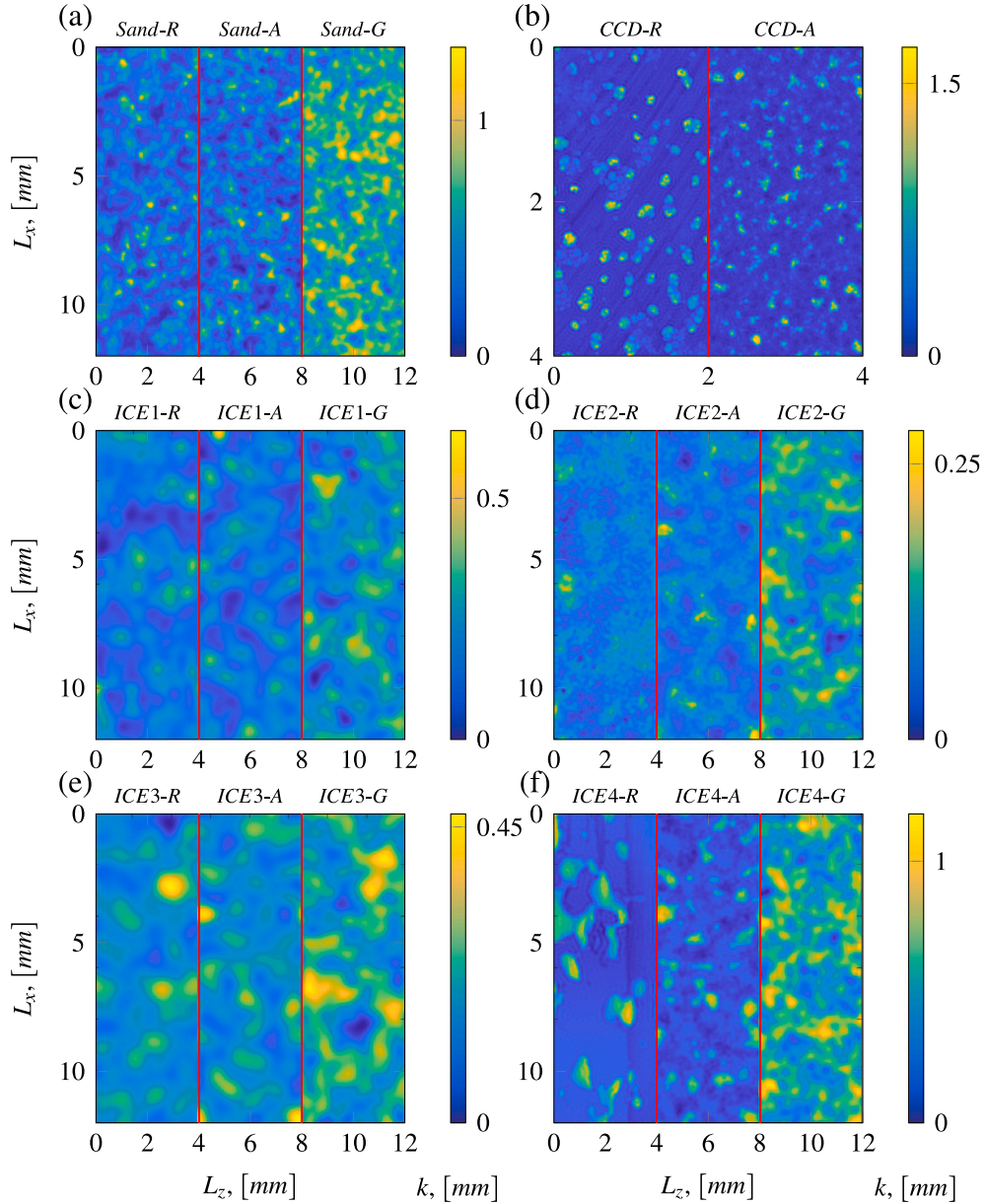


Fig. 4. Overview of the realistic rough surfaces along with their artificial surrogates.

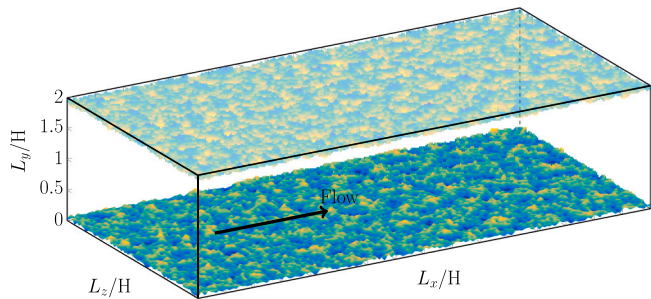


Fig. 5. Schematic representation of simulation domain with an exemplary pseudo-realistic surface mounted on the channel walls. H denotes the channel half height.

2.3. Direct numerical simulations

The DNS is carried out in a fully developed turbulent channel bounded by rough upper and lower walls. An exemplary sketch of the simulation domain is shown in Fig. 5. The flow is driven by CPG. The friction Reynolds number is defined as $Re_\tau = u_\tau(H - k_{md})/\nu$, where $u_\tau = \sqrt{\tau_w/\rho}$ and $\tau_w = -P_x(H - k_{md})$ are the friction velocity and mean wall shear stress, respectively. H is the half distance between the two ‘bottom walls’ of the channel, corresponding to the height of the deepest troughs on each side. The Navier–Stokes equations and energy conservation equation are solved using the pseudo-spectral solver SIMSON (Chevalier et al., 2007), where wall-parallel directions are discretized equidistantly with Fourier polynomial, while in wall-normal direction Chebyshev discretization is employed. The Navier–Stokes equation and the energy conservation equation for the temperature field θ as a dimensionless passive scalar writes:

$$\nabla \cdot \mathbf{u} = 0, \tag{2}$$

$$\frac{\partial \mathbf{u}}{\partial t} + \nabla \cdot (\mathbf{u}\mathbf{u}) = -\frac{1}{\rho} \nabla p + \nu \nabla^2 \mathbf{u} - \frac{1}{\rho} P_x \mathbf{e}_x + \mathbf{f}_{IBM}, \tag{3}$$

Table 2

Simulation configurations. * is the wildcard that represents *R* (realistic), *A* (artificial) and *G* (Gaussian) case. The word in the brackets indicates the domain size configuration — Mini and Full stand for minimal channel and full-span DNS, respectively.

Roughness	Re _τ	H, [mm]	L _x /H	L _z /H	N _x	N _z	N _y	Δ _x ⁺	Δ _z ⁺	λ ₀ /H	λ ₁ /H
ICE1-* (Mini)	500	5	4.0	0.8	512	96	401	3.9	4.2	0.8	0.06
	750	5	4.0	0.8	800	160	401	3.8	3.8	0.8	0.06
	900	5	4.0	0.8	960	192	401	3.8	3.8	0.8	0.06
	1000	5	4.0	0.8	1024	192	401	3.9	4.2	0.8	0.06
ICE2-* (Mini)	500	5	4.0	0.8	1024	192	401	2.0	2.1	0.8	0.02
	1000	5	4.0	0.8	1024	192	401	3.9	4.2	0.8	0.02
	1500	5	4.0	0.8	1200	240	401	5.0	5.0	0.8	0.02
	2000	5	4.0	0.8	1200	240	401	6.7	6.7	0.8	0.02
ICE3-* (Mini)	500	5	4.0	0.8	512	96	401	3.9	4.2	0.8	0.06
	750	5	4.0	0.8	800	160	401	3.8	3.8	0.8	0.06
	1000	5	4.0	0.8	1024	192	401	3.9	4.2	0.8	0.06
	1200	5	4.0	0.8	1152	256	401	4.2	3.8	0.8	0.06
1500	5	4.0	0.8	1200	240	401	5.0	5.0	0.8	0.06	
ICE4-* (Mini)	500	5	4.0	0.8	1024	192	401	2.0	2.1	0.8	0.02
Sand-R (Full)	500	12.8	5.5	3.9	768	384	385	3.6	5.0	0.8	0.02
	500	12.8	6.3	3.1	768	384	385	4.2	4.2	0.8	0.02
Sand-A (Full)	500	12.8	6.3	3.1	768	384	385	4.2	4.2	0.8	0.02
Sand-R (Mini)	500	12.8	4.0	0.8	540	108	385	3.7	3.7	0.8	0.02
Sand-A (Mini)	500	12.8	4.0	0.8	540	108	385	3.7	3.7	0.8	0.02
Sand-G (Mini)	500	12.8	4.0	0.8	540	108	385	3.7	3.7	0.8	0.02
CCD-R (Full)	500	10	6.0	4.0	864	576	401	3.5	3.5	4	0.05
CCD-A (Full)	500	10	6.0	4.0	864	576	401	3.5	3.5	4	0.05

$$\frac{\partial \theta}{\partial t} + \nabla \cdot (\mathbf{u}\theta) = \alpha \nabla^2 \theta + Q + \mathbf{f}_\theta, \quad (4)$$

where ρ , ν , α represent the density, the kinematic viscosity and the thermal diffusivity of the flow, respectively. The double-averaged velocity and temperature profiles in wall-parallel directions and time are denoted as U and Θ for the sake of simplicity. $P_x = (1/\rho)dP/dx$ and $Q = -ud\Theta/dx$ represent the constant pressure gradient and the temperature source, respectively.

The constant temperature $\theta = 0$ is applied on the lower and upper wall, while a source term is added to the conservation equation in order to achieve a developed temperature field. Immersed boundary method (IBM) based on Goldstein et al. (1993) is used to impose the no-slip and constant temperature boundary condition to the rough surface by introducing external source term to the momentum (\mathbf{f}_{IBM}) and energy (\mathbf{f}_θ) equation. The constant Prandtl number is set to $Pr = 0.71$.

Due to the high computational cost of conventional DNS, we partially utilize the minimal channel configuration (termed *Mini*) for predicting flow and temperature field over roughness as proposed by Chung et al. (2015) and MacDonald et al. (2019). The technique has been recently examined in details and proven to be suitable for irregular roughness by Yang et al. (2022, 2021). These works show that in a small simulation domain the turbulent flow in the near wall region up to the critical height $y_c^+ = 0.4L_z^+$ can be considered as 'healthy turbulence' (Chung et al., 2015). In this region the flow is deemed physical.

The physical scaling of the channel half height H is selected for each case individually to achieve a clear separation of length scales H and k while maintaining a significant roughness effect within the current range of Re_τ . Among other cases, the H for the *Sand* cases is selected to be consistent with the experiment facility at the Institute of Fluid Mechanics, KIT (von Deyn et al., 2022). The largest and smallest roughness wavelengths λ_0 and λ_1 of each type of roughness are selected individually to resolve as much roughness length scales that are influential for the roughness effect to the flow as possible. The simulation grid size criteria with $\Delta_x \approx \Delta_z \lesssim \lambda_1/4$ is applied for all simulations, where Δ_x and Δ_z represent wall-parallel grid sizes in streamwise and spanwise direction, respectively. The extent of the simulation domain is selected to accommodate for the largest roughness wavelength, i.e. with $L_z \geq \lambda_0$. A summary of the currently investigated cases along with the their corresponding simulation configurations is provided in the Table 2.

3. Results

3.1. Global flow statistics

An analysis of the global flow properties, i.e. the skin friction coefficient C_f and the Stanton number St , is possible for the roughness for which DNS in full-span channels is performed — these are the *Sand* and *CCD* roughness. The skin friction coefficient is defined as:

$$C_f = \frac{2\tau_w}{\rho U_b^2} = \frac{2}{U_b^{+2}}. \quad (5)$$

Where $U_b = \int_0^{2H} U dy / (2H - 2k_{\text{md}})$ is the bulk velocity. The heat transfer rate can be quantified by the Stanton number St , which is defined as:

$$St = \frac{1}{U_b^+ \Theta_m^+}, \quad (6)$$

where $\Theta_m = \int_0^{2H} U(\Theta - \Theta_w) dy / \int_0^{2H} U dy$ is the mixed mean temperature (Pirozzoli et al., 2016) and Θ_w represents the wall temperature.

The mean velocity and temperature profiles over these rough surfaces are shown in Fig. 6. It is noteworthy that the artificially generated roughness are subjected to the randomness introduced by the generation algorithm. Thus, the realizations of the individually generated artificial roughness are different although they are generated based on identical PDF and PS. Nonetheless, the previous investigations (Yang et al., 2022, 2021) have demonstrated that the randomness introduced by the present random roughness generation algorithm has a negligible impact on the roughness hydrodynamics and thermal properties. Therefore, the artificial surfaces in the present work are regarded as reliable instances that represent the flow properties of roughness with desired PDF and PS. The empirical log-law for the mean velocity profile over smooth surface is included in Fig. 6(a) as a reference for the smooth channel simulations:

$$U^+ = \frac{1}{\kappa} \log(y^+) + B, \quad (7)$$

where $\kappa = 0.4$ is the von Kármán constant and $B = 5.2$ is the smooth wall intercept. The virtual origin of the rough wall is determined by the zero-plane displacement d following Jackson's method (Jackson, 1981) in the current work.

It can be seen in Fig. 6, that the profiles of the artificial surfaces collapse well to their target realistic counterparts. As a result, the maximum error of C_f and St lower than 3% is achieved for the artificially generated roughness *Sand-A* and *CCD-A* as indicated in the Table 3. As mentioned before, minimal channel DNS is employed for study of ice accretion samples in this work. To demonstrate how this approach performs, we additionally conducted a minimal channel simulation for *Sand-R* as well as a smooth minimal channel, which are further included in Fig. 6 with dash-dotted line pattern. The critical height of the minimal channel $y_c^+ = 160$ is marked with the vertical red dashed line. It is evident that the mean flow and temperature profile in the minimal channel agree well with the conventional full-span channel results up until the critical height y_c^+ in logarithmic layer. The departure of the mean velocity as well as the mean temperature profiles for minimal channels can be observed in the outer region. This can be attributed to limited spanwise width of the minimal channel. The structures larger than the spanwise size of the channel are not captured in the outer layer, leading to a build up of undissipated kinetic energy (Jiménez and Moin, 1991). This translate to the overshoot of the mean profiles in the outer region beyond y_c . This observation, in line with the results already reported in Yang et al. (2022), shows that the roughness-induced offset in the mean velocity and temperature profiles can be well reproduced using DNS in a minimal channels. The comparison of artificial and realistic roughness, presented in the following sections, is based on minimal channels.

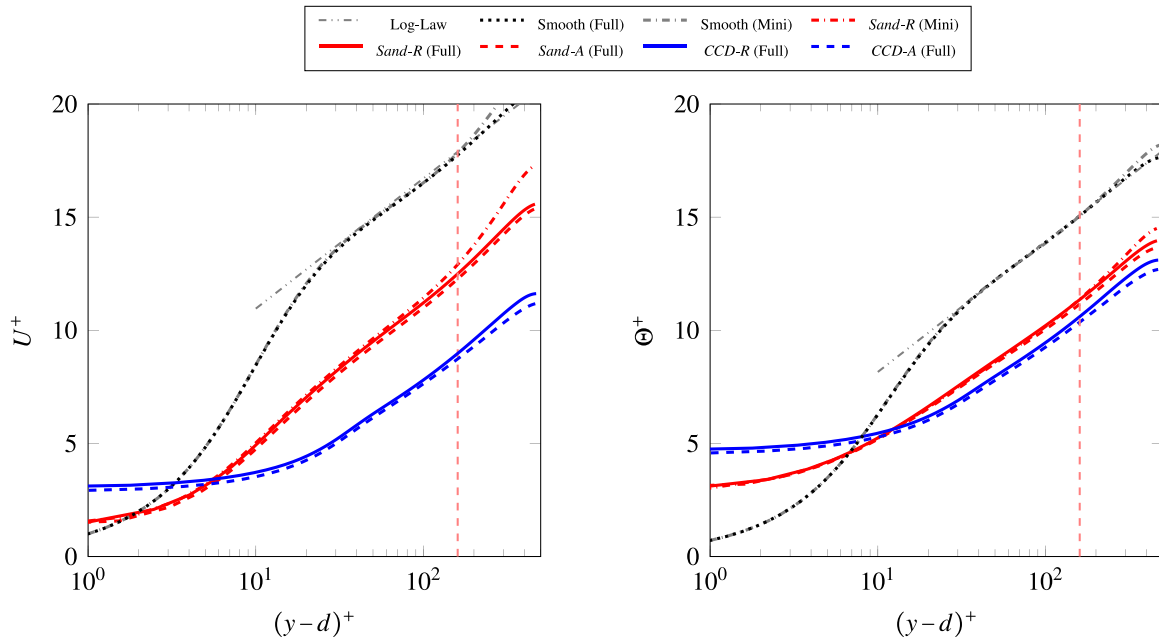


Fig. 6. Mean velocity and temperature profiles at $Re_\tau = 500$. The critical height y_c^+ for the minimal channel is marked with red vertical dashed line. The temperature log-law is based on Kader (1981).

Table 3
Global flow statistics obtained from full-span channel simulations.

Flow statistics	<i>Sand - R</i>	<i>Sand - A</i>	<i>CCD - R</i>	<i>CCD - A</i>
C_f	0.0138	0.0134	0.0266	0.0268
St	0.0068	0.0069	0.0036	0.0036

3.2. Mean velocity and temperature profiles

The inner-scaled mean velocity and temperature profiles of all artificial roughness in minimal channels, i.e. *ICE1-A/G* to *ICE4-A/G* and *Sand-A/G*, at $Re_\tau = 500$ are depicted in Fig. 7. The target roughness, i.e. *ICE1-R* to *ICE4-R* and *Sand-R*, are included in the same plots with solid lines. As can be seen in the figure, the artificial surfaces successfully reproduce the mean velocity and temperature profiles associated with realistic roughness for all roughness except *ICE4*, which will be discussed separately. It is remarkable that all the Gaussian artificial surfaces do not show a considerable deviation from the original non-Gaussian realistic surfaces beyond the region very close to the wall. This results in an almost identical ΔU^+ value between the non-Gaussian and Gaussian artificial surfaces with the same PS. The *Sand* roughness is the exception to this observation. This observation, while puzzling at the first sight, can be attributed to the low ES of the first three samples (see Table 1). It has already been shown by Forooghi et al. (2017) that at low ES, the roughness function is much less sensitive to the moments of PDF. The fact that the Gaussian and non-Gaussian profiles of *Sand* roughness, which has a considerably larger ES, do not collapse agrees with this explanation too. Further evidence of this conjugated correlation can be found in the previous research by Lee et al. (2022). In their work, predominant role of the surface statistics $Sk \times ES$ in determining the roughness skin friction is reported through the sensitivity analysis on a machine learning model trained for predicting the roughness equivalent sand grain height. In light of the observations by Barros et al. (2018), it is possible to draw a physical explanation: roughness with low ES value falls under the so-called ‘wavy’ regime (Schultz and Flack, 2009), in which regime the roughness induced pressure drag is less pronounced compared to the frictional drag. Thus, the pressure drag contribution by the roughness peaks is less dominant to the surface drag. As a consequence, the

resultant roughness skin friction is less sensitive to the change of the roughness height distribution — which is represented by the shape of PDF. As mentioned, for all samples, however, the mean profiles very close to the wall do not agree. This can be due to the significantly altered volume occupation of the Gaussian artificial roughness.

Despite the excellent performance of other artificial roughness, *ICE4-A* is unable to reproduce the realistic mean velocity and temperature profiles with a significantly larger offset in the mean velocity profile than *ICE4-R*. An obvious explanation can be the strong anisotropic nature of this roughness that cannot be reproduced by the present isotropic approach. Busse et al. Busse and Jelly (2020) reported that an isotropic roughness aggravates the roughness disturbance by breaking the ‘streamwise-channeling’ effect comparing to the streamwise elongated structures of realistic surface.

3.3. Reynolds stresses

The Reynolds stresses of all investigated roughness at $Re_\tau = 500$ are visualized in Fig. 8, roughness crest height k_t and the critical height of minimal channel y_c^+ are indicated with gray and red vertical dash lines, respectively. Note that the *CCD* surfaces are simulated in a full-span channel with no critical height. The corresponding Gaussian artificial surface is shown in each plot as well for comparison. It is clear that for all cases, but *ICE4*, the artificial roughness (dashed lines) successfully reproduced the Reynolds stress profiles, while Reynolds stresses of Gaussian artificial surfaces (dotted lines) fails to reproduce the peak value and shows considerable deviation below the roughness crest $y < k_t$. This is arguably attributed to the flow blockage effect of the surface which is manipulated by the PDF configuration. Note that the Gaussian artificial surface has an increased k_{md} values (measured from the bottom wall), which possibly contributes to this deviation and the fact that the peaks of the Reynolds stresses are moved away from the bottom wall. The Reynolds stresses from full span channel simulation of *Sand-R* are included in Fig. 8(e) with gray squares. While the Reynolds stresses show excellent agreement among *Sand-R/A* surfaces below the critical height y_c^+ , slight departure of the Reynolds stress profiles can be observed for the *Sand-R* between minimal channel and full-span channel simulations beyond the critical height y_c due to the nature of minimal channel. For all the cases considered in the present work, the

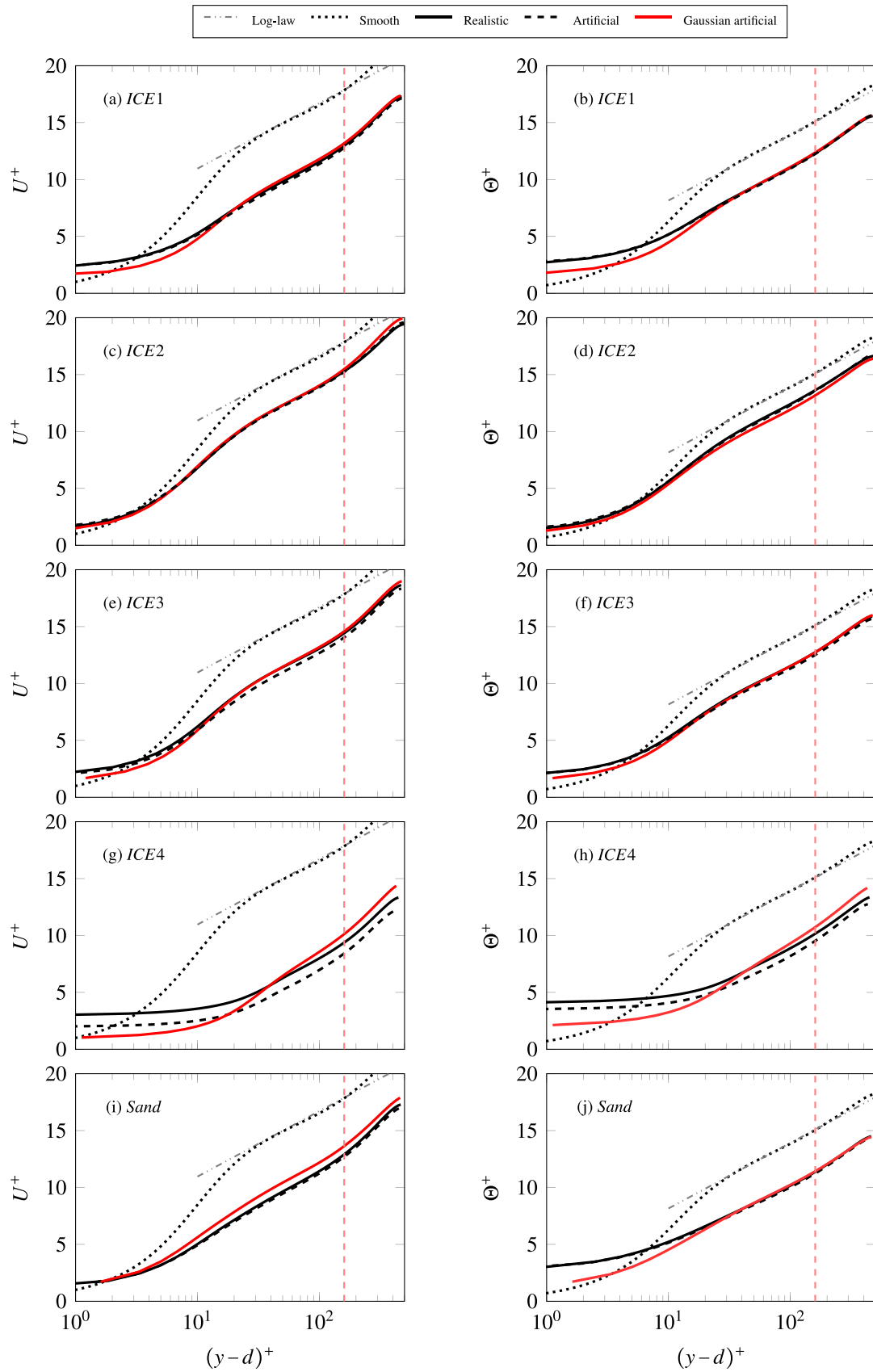


Fig. 7. Mean velocity and temperature profiles at $Re_\tau = 500$ in minimal channels. The vertical dashed line represents the critical height of the minimal channel $y_c^+ = 160$. (a,c,e,g,i): mean velocity profiles ΔU^+ , (b,d,f,h,j): mean temperature profiles θ^+ . The temperature log-law is based on Kader (1981).

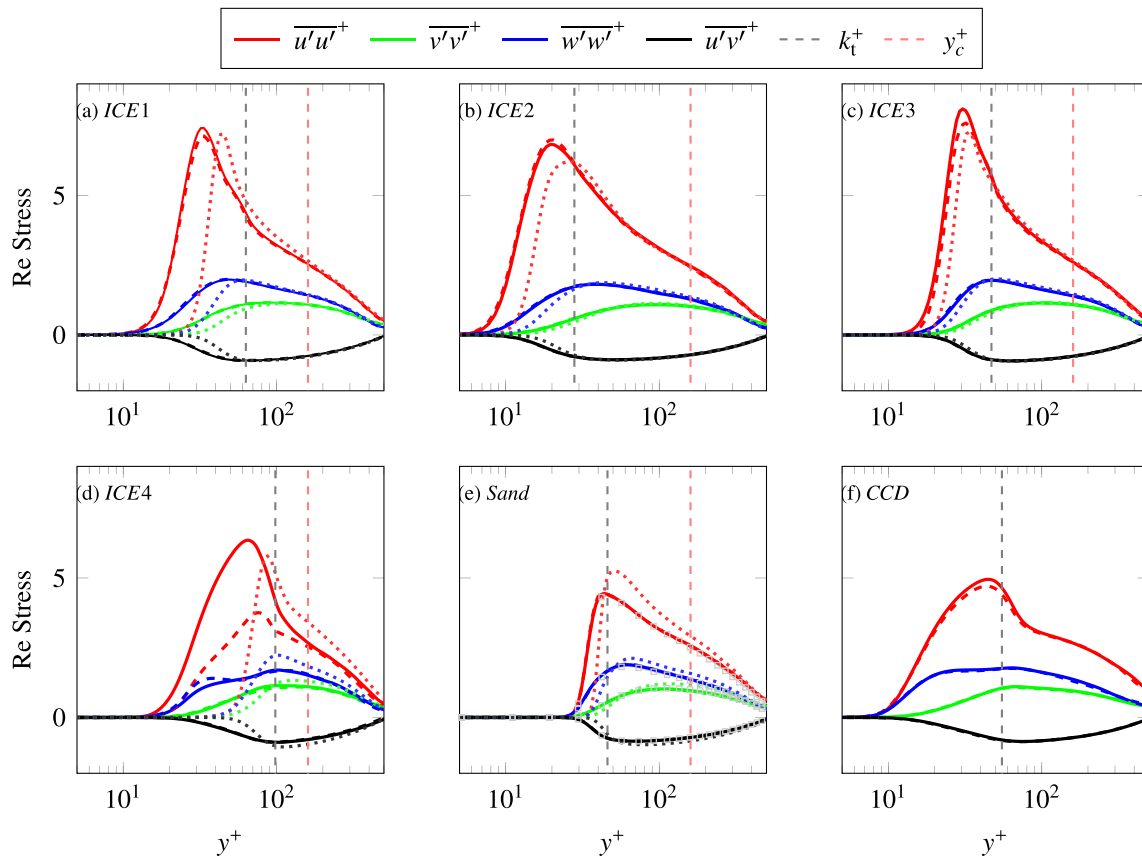


Fig. 8. Reynolds stresses of ICE1 to ICE4, Sand and CCD at $Re_\tau = 500$. The gray vertical dashed line represents k_t^+ of realistic surfaces, the red vertical dashed represents y_c^+ of minimal channel simulations. Solid line: realistic, dashed line: artificial, dotted line: Gaussian. In (e), Full-span channel DNS results of Sand-R are included in the plot with gray squares.

Table 4
Equivalent sand-grain height of realistic and artificial surfaces, unit: mm.

k_s	ICE1	ICE2	ICE3
Realistic	0.38	0.30	0.35
Artificial	0.40	0.30	0.35

peaks of streamwise Reynolds stresses locate below the roughness crest k_t .

Similar to the mean profiles, the artificial roughness ICE4-A fails to reproduce the Reynolds stresses. As discussed in the previous section, the considerable discrepancies of the roughness effect is due to the isotropic assumption of the artificial roughness. As one can see from the profile of streamwise normal Reynolds stress $\overline{u'u'^+}$, realistic roughness yields a higher $\overline{u'u'^+}$ peak value compared to the artificial isotropic roughness. This is likely due to the fact that realistic roughness shows surface anisotropy and are prone to form quasi-streamwise vortices. This finding is in agreement with the work by Busse and Jelly (2020). In contrast, roughness anisotropy shows less impact on other Reynolds stresses. Among others, spanwise Reynolds stress $\overline{w'w'^+}$ shows slight increase in the near wall region for artificial isotropic roughness. This could be the consequence of the increased spanwise interference in comparison to the realistic rough surface.

3.4. Equivalent sand-grain height

As indicated in the previous sections, satisfactory results are obtained for the reproduced roughness at $Re_\tau = 500$. However, the roughness likely lies in transitionally rough regimes at the present Re_τ . In order to ensure that the artificial surfaces hold comparable

performance to their target surfaces in fully rough regime too, Re_τ is extended up to the fully rough regime for successfully reproduced cases in minimal channels, i.e. ICE1 to ICE3. Using the data at fully rough regime, it is possible to calculate the equivalent sand-grain height k_s for different realistic and artificial samples. In order to calculate the k_s values, roughness function ΔU^+ for each roughness at different Re_τ is evaluated. The ΔU^+ values in the present work are calculated by subtracting the mean inner-scaled velocity profile over roughness from the value obtained from Eq. (7) (smooth wall) at $y_c^+ = 160$.

The values of roughness function ΔU^+ are plotted in Fig. 9(a) as functions of roughness height k_{99}^+ for the case ICE1-A to ICE3-A with squares. Here k_{99} is the 99% confidence interval of the roughness PDF. The realistic surfaces ICE1-R to ICE3-R are represented by triangles. All the surfaces exhibit fully-rough behavior at adequately high Re_τ . They collapse to a single logarithmic function (Nikuradse, 1930) for uniform sand grain. To complete the comparison, the ΔU^+ values of ICE4-R and ICE4-A at $Re_\tau = 500$ are additionally included in Fig. 9(a) with black triangle and square, respectively. The ICE4-A surface yields a disagreement in ΔU^+ of 13%. The equivalent sand-grain height k_s of the ICE1 to ICE3 surfaces are obtained by aligning the roughness function in fully rough regime with the experiments, i.e. with the empirical equation:

$$\Delta U^+ = \frac{1}{\kappa} \ln(k_s^+) + B - 8.48. \quad (8)$$

The roughness function against calculated k_s^+ values are shown on the right panel of Fig. 9, also included are the experiments by Nikuradse (1930) and Moody (1944). The figure shows that each pair of artificial and realistic roughness produce very similar values of ΔU^+ . It is also observed that, in the transitionally rough regime the variation

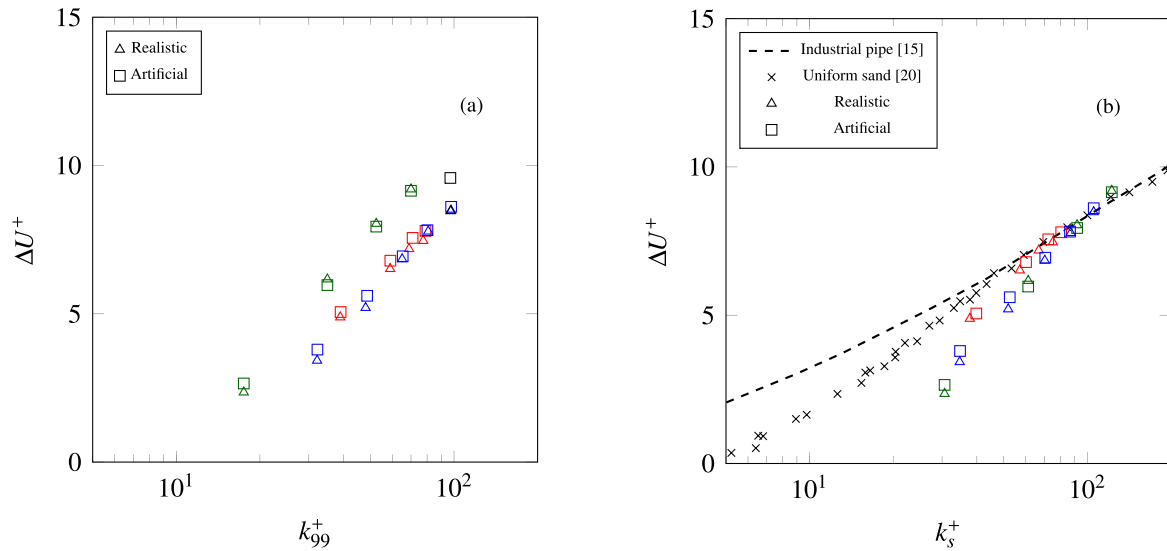


Fig. 9. Roughness functions of different roughness with varying Re_τ as functions of k_{99}^+ (a) and k_s^+ (b). Red: ICE1 ($k_s = 0.38$ mm vs. 0.40 mm), green: ICE2 ($k_s = 0.30$ mm), blue: ICE3 ($k_s = 0.35$ mm) and black: ICE4. It should be noted that the black triangle overlaps with the blue triangle at $k_{99}^+ \approx 100$. (For interpretation of the references to color in this figure legend, the reader is referred to the web version of this article.)

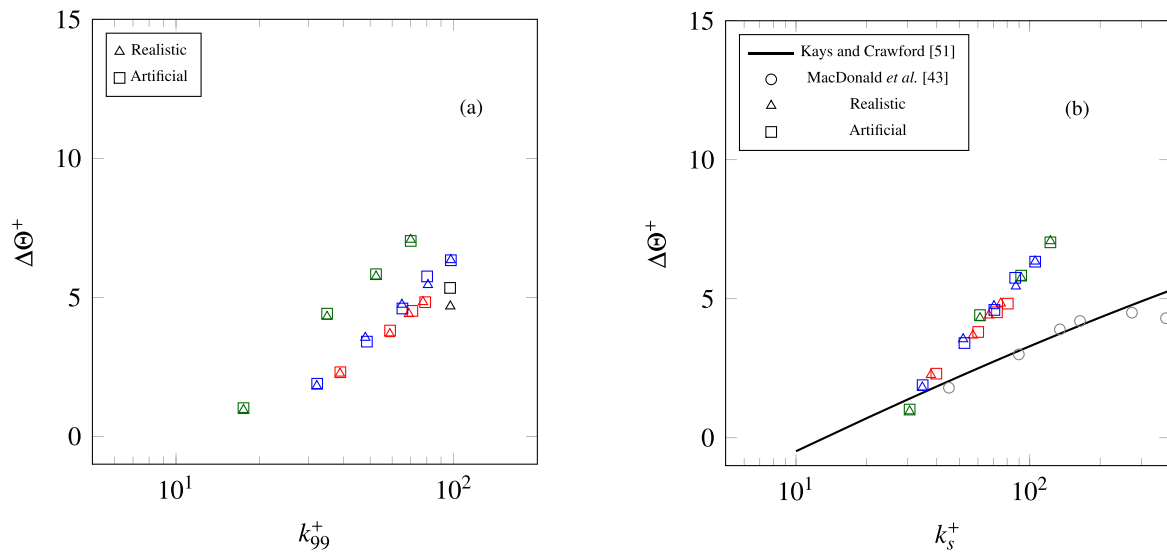


Fig. 10. Temperature roughness functions of different roughness with varying Re_τ as functions of k_{99}^+ (a) and k_s^+ (b). Red: ICE1, green: ICE2, blue: ICE3 and black: ICE4.

of ΔU^+ against k_s^+ for ICE1 to ICE3 roughness do not follow that of the Nikuradse sand-grain roughness (Nikuradse, 1933), and steeper transition to the fully rough regime can be observed. The identical transition behavior between each pair of realistic and artificial surfaces indicates the consistency of the roughness flow properties. The considered ICE1 to ICE3 surfaces reach fully rough at approximately $60 < k_s^+ < 80$. Overall the results in Fig. 9 and Table 4 indicate that the pseudo-random roughness with matched PDF and PS can be a suitable surrogate for realistic roughness when it comes to the investigations of equivalent sand-grain roughness k_s .

The temperature roughness functions $\Delta \Theta^+$ are calculated by subtracting the mean inner-scaled temperature profile over roughness from the value obtained from the empirical log-law of the smooth wall for temperature profile (Kader, 1981),

$$\Theta^+ = \frac{Pr_t}{\kappa} \ln(y^+) + \beta(Pr), \quad (9)$$

where $Pr_t = 0.85$ is the turbulent Prandtl number and the empirical function $\beta(Pr)$ writes

$$\beta(Pr) = (3.85 Pr^{1/3} - 1.3)^2 + \frac{Pr_t}{\kappa} \ln Pr. \quad (10)$$

In Fig. 10, temperature roughness functions for ICE samples are plotted against k_{99}^+ and k_s^+ on the left and right panels, respectively. The first observation is a very good agreement between realistic and artificial temperature roughness functions for ICE1-3. Considerable discrepancy ($\approx 14\%$) for ICE4 - A in terms of $\Delta \Theta^+$ is observed, which can be attributed to the surface anisotropy as discussed above. On the right panel of Fig. 10, we also observe a surprising collapse of data when $\Delta \Theta^+$ is plotted against k_s^+ . One must keep in mind that unlike ΔU^+ , $\Delta \Theta^+$ is not uniquely determined by k_s^+ and the effect of roughness topography can lead to a certain scatter in data (Chung et al., 2021). However, the roughness samples ICE1 to ICE3 all have very low effective slopes, which can lead to a closer analogy between skin

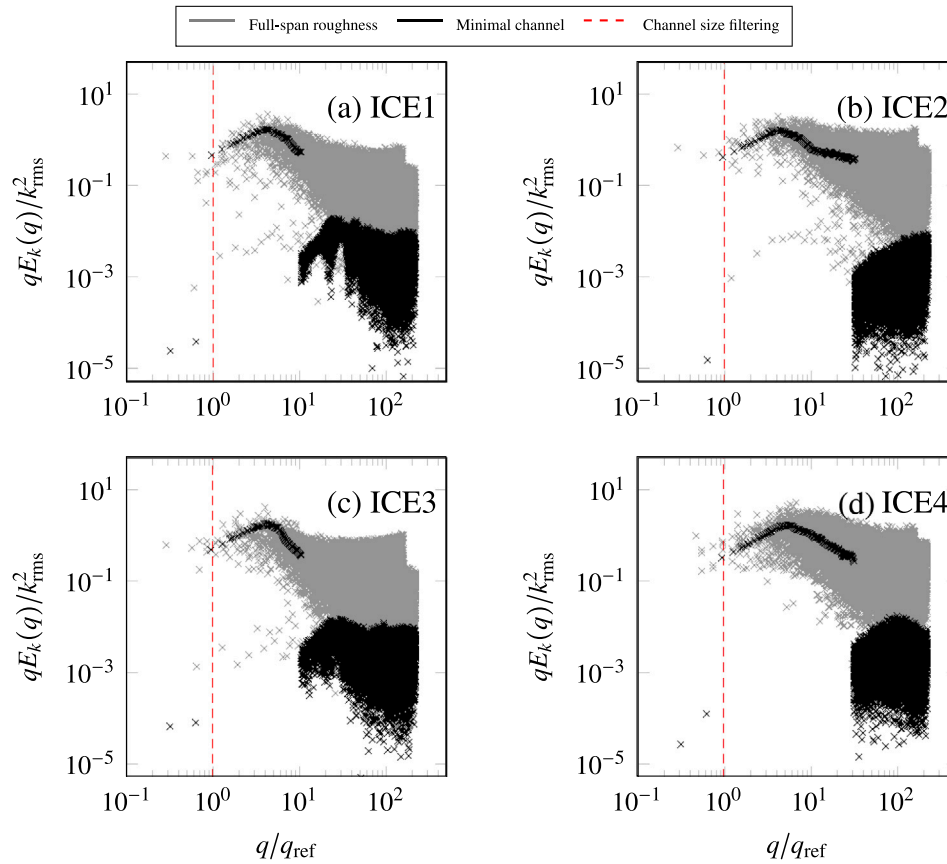


Fig. 11. Pre-multiplied PS of the minimal channel roughness ICE1-4.

friction and heat transfer, hence a good correlation between $\Delta\theta^+$ and k_s^+ .

Additionally, in Fig. 10(b) the empirical correlation proposed by Kays et al. (1980) as well as DNS data of MacDonald et al. (2019) are plotted for comparison. Remarkably, the slope of $\Delta\theta^+$ in the current data is closer to that of ΔU^+ than the empirical correlation for $\Delta\theta^+$. Also the saturation reported by MacDonald et al. is absent here. This is also likely attributed to the low effective slope of the current samples leading to a closer resemblance in the trends of ΔU^+ and $\Delta\theta^+$. Furthermore, the current realistic samples span a range of scales. Due to the delayed onset of the transitionally rough regime for the temperature field (MacDonald et al., 2019) more smaller roughness structures start to behave as thermally rough and contribute to the heat transfer as the Re_τ increases. This possibly translates to the steeper increase of $\Delta\theta^+$ compared with the sinusoidal roughness. Moreover, note that the slope predicted by Kays and Crawford correlation is for roughness in the ‘fully rough’ regime while, as observed in Fig. 9(b), the current cases reach the fully rough asymptote only marginally at the largest Reynolds numbers. Finally the saturation of $\Delta\theta^+$ is observed by MacDonald et al. for a sinusoidal roughness in the fully rough regime. As discussed above, compared to a sinusoidal roughness, the realistic roughness may include length scales smaller than k_s , which can delay $\Delta\theta^+$ reaching an asymptotic constant value. Considering the fact that the saturation of $\Delta\theta^+$ takes place with a slight postpone at $k_s^+ \approx 250$ while the flow reaches fully rough regime at $k_s^+ \approx 150$ for the sinusoidal roughness, the saturation behavior for the ICE surfaces is thus expected at higher k_s^+ value with higher saturation constant value.

4. Conclusions

A mathematical roughness generation method is employed to reproduce realistic rough surfaces based on the PDF and PS of roughness

height. The PDFs and PSs are extracted from 6 types of industrial rough surfaces including ice accretion on aero-engine (ICE), sandpaper (Sand) as well as combustion chamber deposit roughness (CCD), and fed into the roughness generation method. The generated artificial rough surfaces are assessed using DNS in both full-span channels and minimal channels at a wide range of $Re_\tau = 500 - 2000$ to cover both transitionally and fully rough regimes.

The artificial counterparts of the presently considered realistic rough surfaces successfully reproduce both the hydrodynamic and thermal properties of their corresponding roughness as long as the roughness can be considered isotropic. The maximum error in the values of C_f and St is estimated to be less than 3% for the artificial surfaces Sand-A and CCD-A compared to the original surfaces. The artificial surfaces, particularly Sand-A, CCD-A as well as ICE1-A to ICE3-A, are demonstrated to be capable of accurately predicting the mean velocity and temperature profiles as well as the Reynolds stresses. The equivalent sand-grain height k_s^+ of ICE1-A to ICE3-A are calculated, these values are in excellent agreement with their original surfaces. The satisfactory results highlight the promising applicability of the employed roughness generation framework for the future systematic investigation of flow over reality-based irregular roughness surfaces.

Significant deviations in drag and heat transfer is observed for reproducing the strongly anisotropic roughness ICE4-R (SAR ≈ 1.7), as is reflected by the 13% increase of ΔU^+ and 14% increase of $\Delta\theta^+$ of the artificial surface ICE4-A at $Re_\tau = 500$. Furthermore, the decrease of the peak value in the streamwise normal Reynolds stress $\overline{u'u'^+}$ is observed for the artificial roughness ICE4-A compared to the realistic roughness ICE4-R. In light of the present observations, it is estimated that the threshold for a significant streamwise surface anisotropy effect is located at SAR < 1.7 . This value may, understandably, be altered

depending on the interplay of other roughness parameters. A detailed examination of this aspect should be conducted in the future studies.

When the artificial surfaces are generated by only matching the PS and using a Gaussian PDF, considerable departures of the mean flow and temperature profiles are identified in the vicinity of roughness. However, at small Effective Slope values ($ES < 0.2$), it is possible to obtain values of roughness function ΔU^+ with a good accuracy using Gaussian artificial surfaces: however, a considerable decrease of ΔU^+ is observed for the Gaussian artificial surface with $ES > 0.4$, which translates to a lower roughness-induced drag.

Declaration of competing interest

The authors declare that they have no known competing financial interests or personal relationships that could have appeared to influence the work reported in this paper.

Data availability

Data will be made available on request.

Acknowledgments

J.Y. and P.F. gratefully acknowledge partial financial support from the Friedrich and Elisabeth Boysen Foundation, , Germany (BOY-151). This work was performed on the supercomputer Horeka and the storage facility LSDF funded by the Ministry of Science, Research and the Arts, Baden-Württemberg, Germany, and by the Federal Ministry of Education and Research, Germany.

Appendix. Selection of minimal channel spanwise width

For minimal channels, the spanwise width L_z is the main subject of the Chung et al. (2015). The spanwise width of minimal channel acts as the high pass filtering of the roughness structures to exclude roughness wavelengths that are larger than L_z . Although the capability of the minimal channels for *Sand* cases is illustrated, the minimal channel spanwise width setup is closely related to the roughness topographical features, specifically the wall-parallel size of the roughness structures. A L_z value accommodating the dominant roughness wavelengths is essential to ensure the physics of roughness are fully resolved by the shrink simulation domain (Yang et al., 2022). To this end, the pre-multiplied PS of the 4 cases in minimal channel, i.e. ICE1-4-A, are plotted in Fig. 11. As a reference, the PS of the unfiltered original roughness ICE1-4-R are plotted with gray symbols in the corresponding plots. The current selection of the spanwise width, which serves as the high-pass filtering of the roughness is represented by the red dashed line. It is evident that the present configuration of minimal channel successfully resolved the peak of the pre-multiplied PS. On the other hand, a decreasing trend of the coherence function between the roughness wavelength and local surface force is reported by Yang et al. (2022). This indicates that excluding the very large wavelength structures will cause a limited difference to the roughness effect in terms of skin friction. Therefore it is safe to state that the current wavelength filtering will result in a negligible effect to the flow. It is also worth to mention that the aim of the current work is to examine whether PDF and PS can be used as appropriate characterizations of roughness to reproduce the roughness effect. Thus the current selection of channel width should not exert any influence on the conclusion of this study after all.

References

- Anderson, D., Hentschel, D., Ruff, G., 1998. Measurement and correlation of ice accretion roughness. In: 36th AIAA Aerospace Sciences Meeting and Exhibit. American Institute of Aeronautics and Astronautics.
- Anderson, W., Meneveau, C., 2011. Dynamic roughness model for large-eddy simulation of turbulent flow over multiscale, fractal-like rough surfaces. *J. Fluid Mech.* 679, 288–314.
- Bansmer, S., 2020. Aircraft Icing: A Challenging Problem of Fluid Mechanics. Cuvillier Verlag.
- Bansmer, S., Baumert, A., Sattler, S., Knop, I., Leroy, D., Schwarzenboeck, A., Jurkat-Witschas, T., Voigt, C., Pervier, H., Esposito, B., 2018. Design, construction and commissioning of the Braunschweig icing wind tunnel. *Atmos. Meas. Tech.* 11, 3221–3249.
- Barros, J.M., Schultz, M.P., Flack, K.A., 2018. Measurements of skin-friction of systematically generated surface roughness. *Int. J. Heat Fluid Flow* 72, 1–7.
- Bons, J., Taylor, R., McClain, S., Rivir, R., 2001. The many faces of turbine surface roughness. In: ASME Turbo Expo 2001: Power for Land, Sea, and Air. American Society of Mechanical Engineers, V003T01A042–V003T01A042.
- Busse, A., Jelly, T.O., 2020. Influence of surface anisotropy on turbulent flow over irregular roughness. *Flow Turbul. Combust.* 104, 331–354.
- Chan, L., MacDonald, M., Chung, D., Hutchins, N., Ooi, A., 2015. A systematic investigation of roughness height and wavelength in turbulent pipe flow in the transitionally rough regime. *J. Fluid Mech.* 771, 743–777.
- Chan-Braun, C., García-Villalba, M., Uhlmann, M., 2011. Force and torque acting on particles in a transitionally rough open-channel flow. *J. Fluid Mech.* 684, 441–474.
- Chevalier, M., Schlatter, P., Lundbladh, A., Henningson, D., 2007. SIMSON: A Pseudo-Spectral Solver for Incompressible Boundary Layer Flows. KTH Mechanics, Stockholm, Sweden, TRITA-MEK.
- Chung, D., Chan, L., MacDonald, M., Hutchins, N., Ooi, A., 2015. A fast direct numerical simulation method for characterising hydraulic roughness. *J. Fluid Mech.* 773, 418–431.
- Chung, D., Hutchins, N., Schultz, M.P., Flack, K.A., 2021. Predicting the drag of rough surfaces. *Annu. Rev. Fluid Mech.* 53, 439–471.
- Flack, K.A., Schultz, M.P., 2010. Review of hydraulic roughness scales in the fully rough regime. *J. Fluids Eng.* 132 (4), 041203.
- Flack, K.A., Schultz, M.P., Barros, J.M., 2020. Skin friction measurements of systematically-varied roughness: Probing the role of roughness amplitude and skewness. *Flow Turbul. Combust.* 104 (2–3), 317–329, cited By 0.
- Forooghi, P., Stroh, A., Magagnato, F., Jakirlić, S., Frohnäpfel, B., 2017. Toward a universal roughness correlation. *J. Fluids Eng.* 139 (12), 121201.
- Forooghi, P., Stroh, A., Schlatter, P., Frohnäpfel, B., 2018a. Direct numerical simulation of flow over dissimilar, randomly distributed roughness elements: A systematic study on the effect of surface morphology on turbulence. *Phys. Rev. Fluids* 3, 044605.
- Forooghi, P., Weidenlener, A., Magagnato, F., Böhm, B., Kubach, H., Koch, T., Frohnäpfel, B., 2018b. DNS of momentum and heat transfer over rough surfaces based on realistic combustion chamber deposit geometries. *Int. J. Heat Fluid Flow* 69, 83–94.
- Goldstein, D., Handler, R., Sirovich, L., 1993. Modeling a no-slip flow boundary with an external force field. *J. Comput. Phys.* 105 (2), 354–366.
- Hama, F.R., Society of Naval Architects and Marine Engineers, 1954. Boundary-Layer Characteristics for Smooth and Rough Surfaces, By Francis R. Hama.
- Jackson, P.S., 1981. On the displacement height in the logarithmic velocity profile. *J. Fluid Mech.* 111, 15–25.
- Jacobs, T.D.B., Junge, T., Pastewka, L., 2017. Quantitative characterization of surface topography using spectral analysis. *Surf. Topogr.: Metrol. Prop.* 5 (1), 013001.
- Jelly, T.O., Busse, A., 2019. Reynolds number dependence of Reynolds and dispersive stresses in turbulent channel flow past irregular near-Gaussian roughness. *Int. J. Heat Fluid Flow* 80, 108485.
- Jiménez, J., 2004. Turbulent flows over rough walls. *Ann. Rev. Fluid Mech.* 36 (1), 173–196.
- Jiménez, J., Moin, P., 1991. The minimal flow unit in near-wall turbulence. *J. Fluid Mech.* 225, 213–240.
- Kader, B.A., 1981. Temperature and concentration profiles in fully turbulent boundary layers. *Int. J. Heat Mass Transfer* 24 (9), 1541–1544.
- Kawamura, H., Abe, H., Matsuo, Y., 1999. DNS of turbulent heat transfer in channel flow with respect to Reynolds and Prandtl number effects. *Int. J. Heat Fluid Flow* 20 (3), 196–207.
- Kays, W.M., Crawford, M.E., Weigand, B., 1980. Convective Heat and Mass Transfer, Vol. 4. McGraw-Hill New York.
- Kuwata, Y., Kawaguchi, Y., 2019. Direct numerical simulation of turbulence over systematically varied irregular rough surfaces. *J. Fluid Mech.* 862, 781–815.
- Lee, S., Yang, J., Forooghi, P., Stroh, A., Bagheri, S., 2022. Predicting drag on rough surfaces by transfer learning of empirical correlations. *J. Fluid Mech.* 933, A18.
- MacDonald, M., Hutchins, N., Chung, D., 2019. Roughness effects in turbulent forced convection. *J. Fluid Mech.* 861, 138–162.
- Moody, L.F., 1944. Friction factors for pipe flow. *Trans. ASME* 66 (8), 671–677.
- Napoli, E., Armenio, V., De Marchis, M., 2008. The effect of the slope of irregularly distributed roughness elements on turbulent wall-bounded flows. *J. Fluid Mech.* 613, 385–394.

- Nikuradse, J., 1930. Untersuchungen über turbulente strömungen in nicht kreisförmigen Röhren. *Ing.-Arch.* 1 (3), 306–332.
- Nikuradse, J., 1933. Stroemungsgesetze in rauhen Röhren. In: *Forschungsheft* ; 361. VDI-Verl., Berlin.
- Orlandi, P., Leonardi, S., 2006. DNS of turbulent channel flows with two- and three-dimensional roughness. *J. Turbul.* 7, N73.
- Pérez-Ráfols, F., Almqvist, A., 2019. Generating randomly rough surfaces with given height probability distribution and power spectrum. *Tribol. Int.* 131, 591–604.
- Pirozzoli, S., Bernardini, M., Orlandi, P., 2016. Passive scalars in turbulent channel flow at high Reynolds number. *J. Fluid Mech.* 788, 614–639.
- Sarakinos, S., Busse, A., 2022. Investigation of rough-wall turbulence over barnacle roughness with increasing solidity using direct numerical simulations. *Phys. Rev. Fluids* 7, 064602.
- Schlichting, H., 1936. Experimentelle Untersuchungen Zum Rauhgigkeitsproblem. In: *INGENIEUR-ARCHIV*, Verlag nicht ermittelbar.
- Schultz, M.P., Flack, K.A., 2009. Turbulent boundary layers on a systematically varied rough wall. *Phys. Fluids* 21 (1), 015104.
- Scotti, A., 2006. Direct numerical simulation of turbulent channel flows with boundary roughened with virtual sandpaper. *Phys. Fluids* 18 (3), 031701.
- Townsend, A.A., 1976. *The Structure of Turbulent Shear Flow* / A.A Townsend, second ed. Cambridge University Press Cambridge [Eng.] ; New York, p. 429, xi.
- Velandia, J., Bansmer, S., 2019. Topographic Study of the Ice Accretion Roughness on a Generic Aero-Engine Intake.
- Velandia, J.S., Bansmer, S.E., 2020. Detailed atmospheric ice accretion surface measurement using micro-computed tomography. *Atmos. Sci. Lett.* 21 (10), e997.
- von Deyn, L.H., Schmidt, M., Örlü, R., Stroh, A., Kriegseis, J., Böhm, B., Frohnappfel, B., 2022. Ridge-type roughness: From turbulent channel flow to internal combustion engine. *Exp. Fluids* 63, A18.
- Yaglom, A.M., 1979. Similarity laws for constant-pressure and pressure-gradient turbulent wall flows. *Annu. Rev. Fluid Mech.* 11 (1), 505–540.
- Yang, J., Stroh, A., Chung, D., Forooghi, P., 2022. Direct numerical simulation-based characterization of pseudo-random roughness in minimal channels. *J. Fluid Mech.* 941, A47.
- Yang, J., Stroh, A., Jakirlic, S., Frohnappfel, B., Forooghi, P., 2021. Study of irregular roughness in minimal channels. In: *ETMM 13, International Symposium on Engineering, Turbulence, Modelling and Measurement.* 15.09.-17.09.2021.
- Yirtici, O., Ozgen, S., Tuncer, I.H., 2019. Predictions of ice formations on wind turbine blades and power production losses due to icing. *Wind Energy* 22 (7), 945–958.
- Yuan, J., Piomelli, U., 2014. Roughness effects on the Reynolds stress budgets in near-wall turbulence. *J. Fluid Mech.* 760, R1.